Received June 9, 2019, accepted June 17, 2019, date of publication June 24, 2019, date of current version August 22, 2019.

Digital Object Identifier 10.1109/ACCESS.2019.2924493

High-Resolution ISAR Imaging With Sparse Aperture VFM Waveforms Under Low SNR Condition

JIYUAN CHEN[1], LETAO XU[2], XIAOYI PAN[1], PU ZHENG[3], AND SHUNPING XIAO[1]

[1]State Key Laboratory of Complex Electromagnetic Environment Effects on Electronics and Information System, National University of Defense Technology, Changsha 410073, China
[2]Academy of Naval Research, Beijing 100000, China
[3]National Key Laboratory of Science and Technology on Blind Signal Processing, Chengdu 610041, China

Corresponding author: Xiaoyi Pan (mrpanxy@nudt.edu.cn)

This work was supported by the National Natural Science Foundation of China under Grant 61701507, Grant 61571451, and Grant 61890542.

ABSTRACT In recent years, the compressed sensing theory has been widely used in sparse aperture radar imaging. The inverse synthetic aperture radar (ISAR) imaging based on the sparse aperture echo of V-style frequency modulation (V-FM) waveform, which can mitigate the ambiguity appeared in range and velocity, has been proposed in this paper. After analyzing and interpreting the reason why the VFM signal pulse compression needs to use dual channels, we built the VFM waveform sparse echo model and analyze the causes of echo sparseness. A modified weighted compressive sensing (MWCS) algorithm is proposed to obtain high-resolution images under strong noise environment. The innovation of this paper lies in the new weighting method and the iterative reconstruction algorithm. The experimental results are shown to demonstrate the validity of the proposed method.

INDEX TERMS VFM waveform, sparse signal model, ISAR imaging, low SNR condition.

I. INTRODUCTION

The inverse synthetic aperture radar (ISAR) plays an important role in the imaging, recognition and classification of moving targets under all-weather and all-day circumstance [1]–[3]. More new technologies are being used in ISAR imaging, such as MIMO [4]–[8]. In traditional ISAR signal processing, pulse compression techniques and large time-width bandwidth product signals are often used to improve range resolution and detection distance [1]. The intra-pulse frequency modulation waveforms, including linear modulation frequency signal, frequency-stepped signal, have been widely used in modern radar systems [9], [10]. However, a long coherent processing interval (CPI) is required for frequency-stepped waveform to complete the transmission and reception of each burst. Long CPI will generate a relatively large imaging aspect angle, leading to range cell migration. The ''ridge'' ambiguity function of chirp signal will lead to the ambiguity in range and velocity. The ''thumbtack'' ambiguity function of V-style frequency modulation (V-FM) waveform is able to eliminate the ambiguity appeared in range and velocity [11]. It is more conducive to improving the two-dimensional resolution with VFM waveform used in radar system. Some researches about VFM signal characteristic and imaging have been implemented [12]–[15], including dual-channel CS-D algorithm and two-dimensional CS algorithm. But they did not consider the missing observation data in actual situation and the proposed algorithm is sensitive at low signal-to-noise ratio for imaging results. At the same time, few studies have analyzed and explained the causes of the two-channel pulse compression of VFM waveform.

With the continuous development of modern radar systems, more and more functions can be realized by each radar, like multifunction phased array radar, which perform multiple tasks such as target detection, monitoring and tracking within a time window [16], [17]. The authors proposed an adaptive ISAR-imaging-considered task scheduling algorithm in [18], which can allows adaptive allocation of radar resources to the imaging without affecting the execution of other tasks as much as possible. So the aperture of the imaging is discontinuous, which may affect the RD-like imaging algorithm.

The associate editor coordinating the review of this manuscript and approving it for publication was Jinming Wen.

The inevitable interference and jamming in radar system are another reason for the incomplete aperture of echo. Thus, only obtain sparse aperture signal echo can be obtained in a range bin. Compressed Sensing (CS) theory states that the sparse or compressible signals are able to reconstruct exactly from limited measurements by solving a sparsity-constrained optimization problem with a high probability [19]–[21], which is quite suitable to apply to radar imaging [22]–[24]. There are many researches state that sparse aperture signal echo under different waveforms are utilized to reconstruct 2D imaging results by using CS, including LFM signal [25], stepped-frequency waveform [26] and gapped stepped- frequency waveform [27]. However there is few researches on sparse aperture echo imaging of VFM signal.

In the same noise environment, the target echo obtained by the receiver is limited, so the SNR of sparse echo signal is low. Compared with other recovery methods, such as matching pursuit (MP), OMP [28] and SAMP [29], a weighted ℓ_1 minimization method is proposed in [30]. This method outperforms the regular ℓ_1 minimization algorithm mainly in two situations including the required number of measurements to recover a sparse signal is much less and the reconstruction error in noisy environment is significantly reduced. In the conventional weighting method, the constraint on large coefficients is reduced, and the constraint on small coefficients is also reduced. This makes noise suppression less obvious when SNR is low.

This paper focus on sparse aperture VFM waveform ISAR imaging under low SNR condition via modified reweighted compressive sensing. Firstly, the properties of VFM waveform are analyzed and the ISAR imaging using VFM waveform model is formulated, imaging results will become defocused since the missing measurement data. Then, the sparse VFM waveform echo model in cross range domain is proposed and weighted compressive sensing is utilized to recover the signal. In order to overcome the drawbacks of traditional weighted method, we propose a modified weighted method that has a good performance under low SNR condition and the iterative algorithm. Experiments are provided to demonstrate that the framework can achieve high resolution ISAR imaging by using sparse VFM waveform echo under noisy environment.

The remainder of this paper is organized as follows. In section II, the signal model and ISAR imaging processing are introduced, and the sparse signal model and reweighted rule and iterative algorithm are presented in section III. In section IV, several experiments are used to validate the effectiveness of the proposed method. Conclusions are drawn and presented in Section V.

II. ANALYSIS OF VFM WAVEFORM AND IAMAGING MODEL

A. ANALYSIS OF VFM WAVEFORM

V-style frequency modulation (V-FM) waveform refers to a V-style whose frequency changes with time, and its waveform and frequency variation are shown in Fig 1. The VFM signal

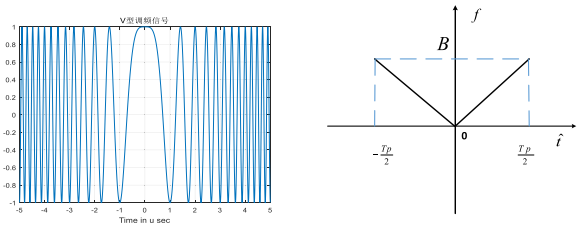

(a) Waveform (b) Sketch map of V-FM waveform

FIGURE 1. Properties of VFM waveform.

can be viewed as two adjacent chirp signals with opposite LFM slopes.

$$s(\hat{t}) = \mathrm{rect}^{-}_{half}\left(\frac{\hat{t}}{T_p}\right)\exp\left(j2\pi\left(f_0 t - \frac{1}{2}\gamma\hat{t}^2\right)\right) + \mathrm{rect}^{+}_{half}\left(\frac{\hat{t}}{T_p}\right)\exp\left(j2\pi\left(f_0 t + \frac{1}{2}\gamma\hat{t}^2\right)\right) \quad (1)$$

where

$$\mathrm{rect}^{-}_{half} = \begin{cases} 1 & \hat{t} \in [-\frac{T_p}{2}, 0] \\ 0 & else \end{cases} \quad \mathrm{rect}^{+}_{half} = \begin{cases} 1 & \hat{t} \in [0, \frac{T_p}{2}] \\ 0 & else \end{cases},$$

γ is the chirp rate, T_p is the pulse duration and bandwidth $B = \gamma T_P$, $\hat{t}$ represents the fast time, and f_0 denotes the frequency of carrier wave, t_m and t represent the slow time and full time respectively, $\hat{t} = t - t_m$. Supposed that the pulse repetition interval (PRI) of radar is T_{PRI}, then $t_m = mT_{PRI}$.

According to the principle of standing phase, we obtain the spectrum of the VFM signal:

$$S(f) = \frac{1}{\sqrt{\gamma}} rect\left(\frac{f - B/2}{B}\right)\left[e^{j\frac{\pi f^2}{\gamma} + j\frac{\pi}{4}} + e^{-j\frac{\pi f^2}{\gamma} - j\frac{\pi}{4}}\right] \quad (2)$$

So the matched filter of VFM signal can be expressed as

$$H(f) = S^*(f)\exp(-j2\pi f t_0) \quad (3)$$

After pulse compression by matching filter, there will be two pulses at the time domain.

$$S_r(f) = S(f)H(f) = \frac{1}{\gamma} rect\left(\frac{f - B/2}{B}\right)\left[e^{j\frac{2\pi f^2}{\gamma} + j\frac{\pi}{2}} + e^{-j\frac{2\pi f^2}{\gamma} - j\frac{\pi}{2}}\right] \quad (4)$$

Thus, in order to solve this problem, dual-channel pulse compression has been proposed for VFM waveform. In this section, we explain why it is necessary to use dual channels to achieve pulse compression from the perspective of the radar signal ambiguity function. The ambiguity function of a signal $s(t)$ is a two dimensional function in Doppler frequency shift ξ and time delay τ define as:

$$\chi_S(\tau, \xi) = \int_{-\infty}^{\infty} s(t)s^*(t - \tau)\exp(j2\pi\xi t)dt \quad (5)$$

where the asterisk refers to the conjugate, a high value of the ambiguity function indicates that it is difficult to resolve two nearby targets whose differences in the time delay and in the

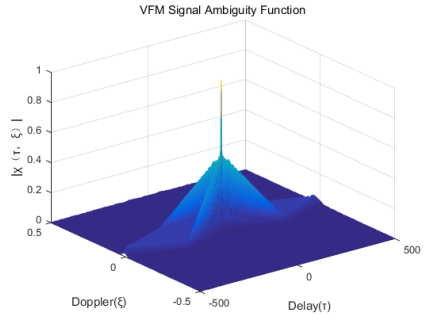

FIGURE 2. Ambiguity diagram of VFM wavefrom.

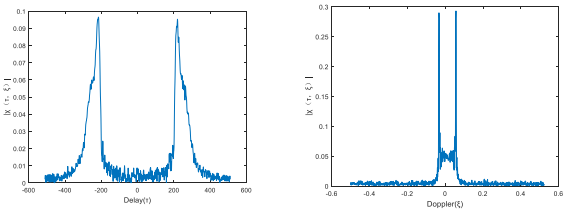

(a) (b)

FIGURE 3. Cutting image along the τ -axis (a) and the ξ -axis (b).

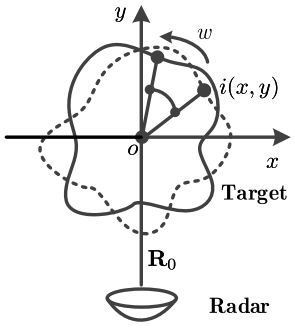

FIGURE 4. ISAR imaging geometric model.

Doppler frequency shift are τ and ξ, respectively. And the ambiguity function of VFM waveform is shown in Fig.2.

In order to explore the traits of the ambiguity diagram more clearly, we cut the ambiguity diagram along the τ-axis and the ξ-axis, shown as fig.3 (a) and (b). When $\xi \neq 0$, the graph cut along the τ axis is decomposed into an approximate sinc function that is symmetric with the ξ axis, and the graph also has two peaks after it is cut along the ξ axis, when $\tau \neq 0$. It means that, when the target is moving, there will be Doppler shift and delay, and the matched filter has no adaptability to the frequency shift. Therefore, it is necessary to consider the two-channel method to realize the pulse compression of the VFM signal.

B. IMAGING MODEL

Supposed that the target's translation motion has been compensated previously, the geometry of monostatic ISAR imaging is illustrated in Fig.4, which is regarded as a turntable imaging model. We set the moving target point o as the origin and give the local coordinate system xoy of moving target. To simplify the process, the y axis is chosen as radar line of light (LOS). Suppose the target makes a circular motion at a fixed angular velocity of w rad/s and the distance from radar to target scatter point o is R_0. The dash line represents the initial position of target, and the solid line represents the position after a rotation angle $\Delta\theta(t)$.

In the case where the observation time (the imaging coherent accumulation time) is short, it can be assumed that the target scattering point moves at a uniform speed in the radar line of sight with respect to the reference point. Suppose the target is located in the far field of the radar field, the instantaneous range from the scattering point $i(x, y)$ to radar during a short CPI can be expressed as

$$\begin{aligned} R(t_m) &= R_0 + x\sin\Delta\theta(t_m) + y\cos\Delta\theta(t_m) \\ &= R_0 + x\Delta\theta(t_m) + y \\ &= R_0 + xwt_m + y \end{aligned} \tag{6}$$

Supposed that σ_i is the scattering coefficient of a scattering point $i(x, y)$ on the moving target. Assume that the target contains I strongest scattering points, the radar echo can be approximated as the following

$$\begin{aligned} s_r(\hat{t}, t_m) &= \sum_{i=1}^{I} \sigma_i s\left(\hat{t} - \frac{2R_i}{c}, t_m\right) \\ &= \sum_{i=1}^{K} \sigma_i \mathrm{rect}_{half}^{-}\left(\frac{\hat{t} - \frac{2R_i}{c}}{T_p}\right) \\ &\quad \times \exp\left(j2\pi\left(f_0\left(t - \frac{2R_i}{c}\right) - \frac{1}{2}\gamma\left(\hat{t} - \frac{2R_i}{c}\right)^2\right)\right) \\ &\quad + \sum_{i=1}^{K} \sigma_i \mathrm{rect}_{half}^{+}\left(\frac{\hat{t} - \frac{2R_i}{c}}{T_p}\right) \\ &\quad \times \exp\left(j2\pi\left(f_0\left(t - \frac{2R_i}{c}\right) + \frac{1}{2}\gamma\left(\hat{t} - \frac{2R_i}{c}\right)^2\right)\right) \end{aligned} \tag{7}$$

where R_i represents the distance from i-th scattering center to the radar, and c is the speed of the electromagnetic wave.

Dual-Dechirping in [14] is used to achieve pulse compression, we use two LFM signals with opposite slopes as reference signals. Each channel is mixed and the remaining video phase is removed. Fourier transform is performed to obtain high range resolution profile (HRRP). One of the channels is flipped and added to the other channel to synthesize HRRP.

$$s(r, t_m) = \sum_{i=1}^{I} T_p\sigma_i \sin c\left(\frac{\gamma T_p}{c}(r - R_\Delta)\right) \times \exp\left(-\frac{j4\pi f_o R_\Delta}{c}\right) \tag{8}$$

where r represents down-range domain, and $R_\Delta = R_i - R_{ref}$, when $R_{ref} = R_0$, substituting (6) into (8), after neglecting the constant phase term, we have the signal in the range cell corresponding to $r = R_\Delta$ as follows [31]:

$$s(t_m) = \sum_{i=1}^{I} T_p\sigma_i \times \exp\left(j2\pi f_{d_i} t_m\right) \tag{9}$$

where $f_{d_i} = 2x_i w/\lambda$ represents the Doppler frequency of i-th scattering point, and λ represents the wavelength.

Applying azimuth FT to (9), we have cross range compression by neglecting the constant phase term

$$s(f_m) = T_p T_a \sum_{i=1}^{I} \sigma_i \cdot \sin c\left(T_a\left(f_m - f_{d_i}\right)\right) \tag{10}$$

where $f_m \in [-f_r/2, f_r/2]$ is the Doppler extent, and f_r is the PRF. The target is resolved in the rang-Doppler (RD) domain, because the cross-range coordinate is proportional to the Doppler frequency. For traditional Fourier Transform method, the RD imaging may defocus when the measured data is too limited to provide sufficient time-spectrum information. In the turntable imaging model, the cross-range resolution is proportional to coherent accumulation time, so a long time observation is necessary. Nevertheless, because the target is uncooperative and maneuvering, it is difficult to collect long-time data. It is most critical that multifunction radar serves different tasks simultaneously, there are very few schedulable resources for imaging, so getting a long-time and complete observation is impossible. This motivates the study of high resolution with limited data.

III. SPARSE SIGNAL MODEL AND RECONSTRUCTION ALGORITHM

A. SPARSE SIGNAL MODEL

Compressed Sensing theory can reconstruct sparse signals with high probability from limited measurement data, which greatly reduce the need for measurement data and cost. Before performing signal sparse representation and reconstruction, we first briefly review the theory of compressed sensing. Let $\mathbf{y} \in \mathbf{C}^M$ denote a finite signal of interest and a basis matrix $\mathbf{\Phi} = \{\varphi_1, \varphi_2, \ldots, \varphi_M\}$. The initial signal can be sparsely represented by a basic matrix, which satisfies $\mathbf{y} = \sum_{i=1}^{M} \varphi_i \theta_i = \mathbf{\Phi}\boldsymbol{\theta}$, where $\boldsymbol{\theta}$ is a vector. If there are only K non-zero values in the vector $\boldsymbol{\theta}$, then the sparsity of the signal $\mathbf{y}$ in the base $\mathbf{\Phi}$ is K. The measurement signal vector can be reduced from M to $\bar{M}$ by the measurement matrix, $\mathbf{s} = \mathbf{A}\mathbf{y}$, where $\mathbf{A} \in C^{\bar{M} \times M} (\bar{M} < M)$ is the measurement matrix. The number of measurements must satisfy $\bar{M} \geq O(K \cdot \log M)$ to achieve optimal recovery for $\mathbf{y}$. So the compression dictionary can be expressed as $\mathbf{\Psi} = \mathrm{A}\mathbf{\Phi}$, which satisfies the restricted isometry constant(RIC) $\delta_K \in (0, 1)$.

$$(1 - \delta_K) \|\boldsymbol{\theta}\|_2^2 \leq \|\mathbf{\Psi}\boldsymbol{\theta}\|_2^2 \leq (1 + \delta_K) \|\boldsymbol{\theta}\|_2^2 \tag{11}$$

Solving the ℓ_0 norm is an NP problem, which has been proved to be equivalent to a convex optimization process.

$$\min\left(\|\boldsymbol{\theta}\|_1\right), s.t. \|\mathbf{s} - \mathbf{\Psi}\boldsymbol{\theta}\|_2 \leq \varepsilon \tag{12}$$

where $\|\|_1$ and $\|\|_2$ represent the ℓ_1, ℓ_2 norm, respectively. min () denotes the minimization, and ε is the noise level. In the actual scene, the ISAR image occupies only a small portion of the entire imaging plane, so the image is sparse. Measurement noise and environmental noise are present during the measurement, so the measured echo data includes the target reflected signal and noise. Therefore the signal in a range cell can be expressed as:

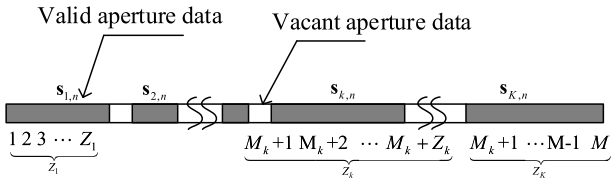

FIGURE 5. Sparse aperture signal vector geometry in the n-th range bin.

$$\mathbf{s} = \sum_{i=1}^{I} T_p \sigma_i \times \exp\left(j2\pi f_{d_i} \mathbf{t_m}\right) + \mathbf{n} \tag{13}$$

where $\mathbf{n}$ is the additive noise in a range cell, and time sequence is $\mathbf{t}_m = [1 : M]^T \Delta t$, and $[\cdot]^T$ denotes vector or matrix transpose, the pulse number and time interval can be calculated by $M = T_a/\Delta t$ and $\Delta t = 1/f_r$, respectively. Discrete Doppler sequence can be expressed as $\mathbf{f}_d = [1 : Q]^T \Delta f_d, Q = f_r/\Delta f_d$, so the dense dictionary is shown as:

$$\begin{aligned} \mathbf{\Psi} &= \left\{\varphi_1, \varphi_2, \ldots, \varphi_q \ldots, \varphi_Q\right\} \\ \varphi_q &= \exp\left[-j2\pi \cdot \mathbf{f}_d(q) \cdot \mathbf{t}\right], \quad 0 \leq q \leq Q \end{aligned} \tag{14}$$

Finally, (9) can be rewritten as $\mathbf{s} = \mathbf{\Psi}\boldsymbol{\theta} + \mathbf{n}$.

The full aperture data should contain a total of M-bursts with indices from 0 to M-1 in the dataset. However, a multifunction radar system has to switch among different targets and serves different activities (some of them have higher priority) [18], some segments of the received echo signal are missing. On the other hand, undesirable interference or jamming signals also are the reasons for the sparse signal in cross-range domain. As shown in Fig.4, we assume that P sparse aperture signal vectors for a single target, which are extracted from the full aperture data. Z_p bursts from $M_p + 1$to $M_p + Z_p$ are included in the n-th sparse aperture data in the n-th range bin. So the p-th sparse signal vector of n-th range bin can be expressed as [32]:

$$\mathbf{s}_{p,n} = \left[s_n\left(M_p + 1\right) s_n\left(M_p + 2\right) \ldots s_n\left(M_p + Z_p\right)\right] \tag{15}$$

The P sparse aperture signal vector in the n-th range bin is

$$\bar{\mathbf{s}}_n = \left[\mathbf{s}_{1,n}\mathbf{s}_{2,n} \ldots \mathbf{s}_{p,n} \ldots \mathbf{s}_{P,n}\right]^T \tag{16}$$

where $\mathbf{s}_{1,n}, \mathbf{s}_{2,n}, \ldots, \mathbf{s}_{P,n}$ are sub-vectors of $\bar{\mathbf{s}}_n$, whose lengths are $Z_1, Z_2, \ldots, Z_P$ respectively, with $Z_1 + Z_2 + \cdots + Z_K = \bar{M}$. Therefore the discrete sparse echo model can be expressed as

$$\bar{\mathbf{s}}_n = \bar{\mathbf{\Psi}}_n \boldsymbol{\theta}_n + \mathbf{n}_n \tag{17}$$

where the length of the measurement P sparse signal vector $\bar{\mathbf{s}}_n$ is $\bar{M}$, $\bar{\mathbf{\Psi}}_n$ $(\bar{M} \times M)$ is a partial sensing dictionary matrix that extracts from original sensing matrix $\mathbf{\Psi}$ with the size of $M \times M$.

We can use method in (12) to solve the optimization problem in (17) by greedy algorithms or orthogonal matching pursuit. In [30], a novel method for sparse signal recovery through weighted ℓ_1 norm optimization is proposed, this

adaptive adjustment mechanism makes the weighted ℓ_1 norm constraint model accurately approximate the ℓ_0 norm model.

$$\min\left(\|\mathbf{w}\boldsymbol{\theta}\|_1\right) \quad s.t.\ \|\mathbf{s}-\boldsymbol{\Psi}\boldsymbol{\theta}\|_2 \le \varepsilon \tag{18}$$

where $\mathbf{w}$ is the vector of weighted coefficients, and whose elements correspond to positive weight w_i for the i-th component of $\boldsymbol{\theta}$. The weight for the recovery signal can be calculated as

$$w_i = \frac{1}{(|\boldsymbol{\theta}_i| + \xi)} \tag{19}$$

where ξ stands for a very small positive, which prevent w_i from appearing singular values. When $\boldsymbol{\theta}_i$ is small, the corresponding weight w_i is constrained to be large, and the component is further constrained in the corresponding reconstruction process (For the noise component, it is equivalent to applying a certain degree of noise suppression). When $\boldsymbol{\theta}_i$ is large, the corresponding weight is small (For the signal to be reconstructed, this constraint effectively guarantees the fidelity of signal reconstruction). This way narrows the gap between large and small coefficients in the contribution of the objective function. Therefore, the weighting process is equivalent to achieving a balanced penalty for large and small coefficients in the optimization process. In the noisy mode, the model is easier to obtain the optimal sparse solution of the object to be optimized than the conventional ℓ_1 norm model.

The weighted ℓ_1 norm has a good sparse approximation effect, but the adjustment of the parameter ξ causes the weights of the large and small coefficients in the reconstructed signal to change in the same direction. The maximum value of the weight changes greatly due to the difference of ξ, which makes the penalty for the small coefficient change drastically, and the reconstruction result lack stability. To solve the above problems, in next subsection, we propose a new weighting scheme and a novel updating rule to obtain the final results based on [33].

B. MODIFIED WEIGHTED RULE AND RECONGSTRUCTION ALGORITHM

Suppose $\boldsymbol{\theta}^*$ is a k-sparse solution vector whose support set is $\mathbf{T_0}$. In [33], they proposed the following weighting scheme to define w:

$$w_i = \begin{cases} w & if\ i \in T_0 \\ 1 & if\ i \in T_0^c \end{cases} \tag{20}$$

where $\mathbf{T}_0^c$ denotes the complementary set of $\mathbf{T}_0$ in $\{1, 2, \ldots, M\}$ and $0 \le w \le 1$. We adopt the popular reweighted ℓ_1 approach to solve (18):

$$\boldsymbol{\theta}^l = \arg\min_{\boldsymbol{\theta}} f\left(\boldsymbol{\theta}; \mu_l, \mathbf{w}^l\right) = 1/2\|\boldsymbol{\Psi}\boldsymbol{\theta} - s\|^2 + \mu_l\|\mathbf{w}\boldsymbol{\theta}\|_1 \tag{21}$$

where $\mu_l > 0$ denotes the penalty parameter and $\mathbf{w}^l$ is the lth iteration weight vector. $\boldsymbol{\theta}^l$ and $\boldsymbol{\theta}^{l+1}$ are two solution vectors that have been solved. At the same time, we update μ_{l+1} by $\mu_{l+1} = \begin{cases} \alpha_0\mu_l, if\ \beta_l > 1 \\ \beta_l\mu_l, if\ \beta_l \le 1 \end{cases}$ with $\beta_l = \frac{\|\mathbf{w}^l\boldsymbol{\theta}^l\|_1}{\|\mathbf{w}^{l+1}\boldsymbol{\theta}^l\|_1}$. This useful tool YALL1 solver (available at http://yall1.blogs.rice.edu/) is used to solve the optimal problem of(21) in each iteration.

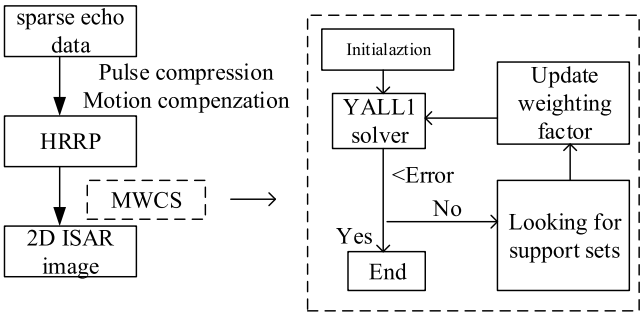

FIGURE 6. The framework of imaging processing.

The size of the $\boldsymbol{\theta}^l$ is obtained by $k_l := \left|\text{supp}\left(\boldsymbol{\theta}^l\right)\right|$. Then we set $\mathbf{d}^l = \boldsymbol{\theta}^l - \boldsymbol{\theta}^{l-1}$ and sort $\mathbf{d}^l$ in decreasing order according to absolute values of its elements:

$$\left|d^l_{j^l_1}\right| \ge \left|d^l_{j^l_2}\right| \ge \ldots \ge \left|d^l_{j^l_{k_l}}\right| \ge \left|d^l_{j^l_{k_l+1}}\right| \ge \ldots \ge \left|d^l_{j_M}\right| \tag{22}$$

We use matrix $\mathbf{N}$ to represent the null space of $\boldsymbol{\Psi}$, and define the ℓ_1-unit sphere in the null space as following:

$$\mathbf{B}_1 = \left\{\mathbf{d} \in \mathbb{C}^M \middle| \mathbf{d} \in \mathbf{N}, \|\mathbf{d}\|_1 = 1\right\} \tag{23}$$

We define $\mathbf{I}(k)$as following:

$$\mathbf{I}(k) = \{S \subset \{1, 2, \ldots, M\} \,||S| \le k\} \tag{24}$$

Then we can get $\mathbf{T}_0$ and $\mathbf{T}_1$ from the following optimization problem:

$$\left(\mathbf{T_0}, \hat{\mathbf{d}}\right) = \arg\max_{\mathbf{T}\in\mathbf{I}(k), \mathbf{d}\in\mathbf{B}_1} \|\mathbf{d}_\mathbf{T}\|_1 \tag{25}$$

$$\left(\mathbf{T_1}, \tilde{\mathbf{d}}\right) = \arg\max_{\mathbf{T}\in\mathbf{I}(k)\setminus\{\mathbf{T}_0\}, \mathbf{d}\in\mathbf{B}_1} \|\mathbf{d}_\mathbf{T}\|_1 \tag{26}$$

Corresponding to $\mathbf{T}_0$ in (25) and $\mathbf{T}_1$ in (26), we further need to define two index sets:

$$\mathbf{T}_0^l = \left\{j_1^l, j_2^l, \ldots, j_{k_l}^l\right\}, \quad \mathbf{T}_1^l = \left\{j_2^l, j_3^l, \ldots, j_{k_l+1}^l\right\} \tag{27}$$

A quantity is defined as follow by using the ratio of optimal objectives mentioned above.

$$\gamma_{\boldsymbol{\Psi}}^l = \frac{\left\|\tilde{\mathbf{d}}^l_{\mathbf{T}_1^l}\right\|_1}{\left\|\hat{\mathbf{d}}^l_{\mathbf{T}_0^l}\right\|_1} \tag{28}$$

Obviously,$0 \le \gamma_{\boldsymbol{\Psi}}^l \le 1$, and $\gamma_l = \xi_1 + \vartheta_l\gamma_{\boldsymbol{\Psi}}^l$, where $\xi_1 < 1$ is a small positive value and $\vartheta_l = \alpha_1\vartheta_{l-1}$ with $\alpha_1 > 1$ and $\vartheta_0 > 0$ being given. This quantity definition is very clear because there are only two optimization issues involved. We can update the weight vector $\mathbf{w}$ by following rule:

$$w_i^{l+1} = \begin{cases} \gamma_l, & if\ i \in \mathbf{T}_0^l \\ \xi_1 + \vartheta_l + \dfrac{1}{|\theta_i^l + \xi_2|}, & if\ i \notin \mathbf{T}_0^l \end{cases} \tag{29}$$

where $0 < \xi_2 \le 1$. So, let's summarize the whole imaging framework shown as Fig.6. The receiver receives sparse target echo information and obtains HRRP after pulse compression and motion compensation. High resolution image can be

obtained by using MWCS algorithm to reconstruct HRRP under the condition of low SNR. In MWCS algorithm, after parameters initialization, YALL1 solver is firstly used to calculate the solution vector. Calculate the error of the solution vector, and then determine whether it meets the requirements, if not, find the support set according to (22) - (27). The weighting coefficient is obtained through (29), and the new solution vector is obtained by using YALL1 solver again. Until the solution vector reaches the error requirement or the maximum iteration number, the final solution vector is obtained. It can be seen from the above derivation and calculation that the support set is closer to the real value after each iteration.

Another concern is the complexity of the algorithm. As shown in [34], for a signal with k nonzero elements, the computational cost of the YALL1 algorithm and l1-regularized least squares algorithm (l1_ls) both are about $O(k \cdot M\bar{M})$, where $M\bar{M}$ is the dimension of the measurement matrix. However, the computational complexity of MWCS algorithm is related to the reconstructed signal. The calculation to find the support set is approximately $O(M)$, and the calculation to update the weighted coefficient is approximately $O(M)$. Therefore, the calculation of updating weighting coefficient is approximately $O(M)$. Finally, the computational complexity of the entire MWCS algorithm is approximately $O\left(kM^2\bar{M}\right)$, which is higher than other algorithms. But the fast GPU parallel implementation would be used to reduce the computation time.

IV. EXPERIMENTS AND ANALYSIS

A. RECONSTRUCTION ALGORITHM PERFORMANCE COMPRESSION

In this subsection, the signal of interest is Gaussian sparse signal with length of $M = 256$, we set the measurement number $\bar{M} = 128$, then we can obtain the partial random Gaussian sensing operator. This experiment investigates the probability of accurate reconstruction of signals with different signal sparsity K under a fixed number of measurements $\bar{M}$. The signal sparsity in this experiment is set from K = 10 to K = 70, for each K, each algorithm simulates 1000 times to calculate the probability of an exact reconstruction.

Another experimental study investigates the probability of accurate reconstruction of signals with different signal measurements for a given signal sparsity K = 20, and we set M $\in$ (50, 55, …, 95, 100). For each K, 1000 experiments were repeated to calculate the probability of accurate reconstruction of the signal. The data measurement number $\bar{M}$ is represented by the x-axis and the probability of signal reconstruction is represented by the y-axis.

The stopping criterion of the proposed algorithm is Error $= \frac{\left\|\boldsymbol{\theta}^l - \boldsymbol{\theta}^{l+1}\right\|}{\max\left\{1, \left\|\boldsymbol{\theta}^l\right\|\right\}} \leq 10^{-2}$, and set $tol = 10^{-4}$ the stopping criterion for YALL1 solver. For initialization, the algorithm set $\boldsymbol{\theta}^0 = 0$ and $\mathbf{w}^1 = (1, 1, \ldots, 1)^T$, and the other parameters are set as $\xi_1 = 10^{-10}$, $\vartheta_0 = 0.1\mu_1\bar{M}/M$, $\alpha_1 = 1.005$, $\alpha_0 = 0.2$, $\mu_1 = 0.01\left\|\boldsymbol{\Psi}^T\mathbf{s}\right\|_\infty$. For $\boldsymbol{\theta}^l$, its components are sorted in decreasing magnitude $\left|\theta^l_{j_1}\right| \geq \left|\theta^l_{j_2}\right| \geq \ldots \geq \left|\theta^l_{j_M}\right|$. Instead of fixing ξ_2 in updating $\mathbf{w}$ in (30), we use ξ_2 as suggested by [30]: $\xi^l_2 = \max\left\{10^{-3}, \left|\theta^l_{j_0}\right|\right\}$ and $j_0 = \left\lceil \frac{\bar{M}}{4\log(M/\bar{M})} \right\rceil$. The definition $\mathbf{T}^l_0$ represents the number of non-zero elements in the vector $\boldsymbol{\theta}^l$. In order to avoid including too many such elements since there are many elements of small magnitude in $\boldsymbol{\theta}^l$, we define $k_l(r) = \min\left\{\eta : \sum_{i=1}^{\eta}\left|\theta^l_{j_i}\right| \geq r\left\|\boldsymbol{\theta}^l\right\|_1\right\}$, where $r \in (0, 1)$ to control the total percentage of the contribution of the first η largest elements (in terms of the magnitude) in $\boldsymbol{\theta}^l$ to its ℓ_1-norm $\left\|\boldsymbol{\theta}^l\right\|$. Via calculation, r is chosen by [33]

$$r_0 = \begin{cases} \dfrac{1}{\ln\left(M/\bar{M}\right)}, & \ln\left(M/\bar{M}\right) > 1 \\ 0.7, & \text{otherwise.} \end{cases}$$

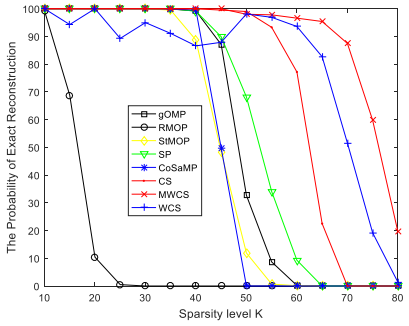

FIGURE 7. The probability of exact reconstruction under different signal sparsity.

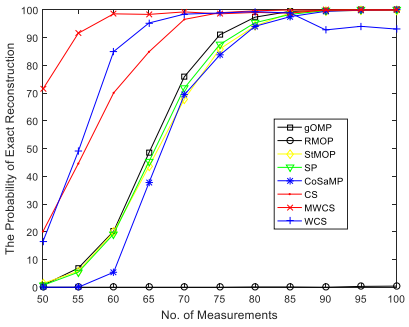

FIGURE 8. The probability of exact reconstruction under different number of measurement.

Fig.7 and Fig.8 demonstrate the results for Gaussian sparse signal under different sparsity and number of measurement. As can be seen, performance of the algorithm we proposed far exceeds other reconstruction algorithm, including the weighted compressive sensing proposed by Emmanuel J. Candes. In Fig.7, while all other algorithms start to fail when sparsity $K > 50$, the MWCS still can afford until sparsity $K > 70$—nearly equal a half of the number of measurements, and have a stable reconstruction performance than WCS. In Fig.8, it is also obvious to observe that MWCS algorithm has better reconstruction performance with fewer measurements. When the measurement quantity exceeds 55, the MWCS method can carry out signal reconstruction with

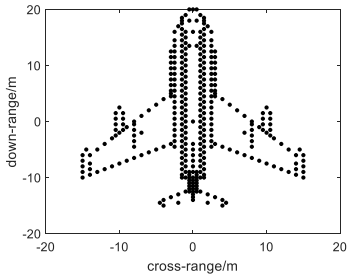

FIGURE 9. Aircraft model.

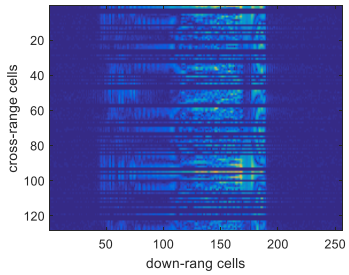

FIGURE 10. Sparse signal.

high probability. In addition, it can be seen from the figure that the signal reconstruction effect of WCS and CS is better than other methods.

B. ISAR IMAGING PERFORMANCE

To verify the performance of proposed method in VFM ISAR imaging, a Yak-42 plane model of 330 point scattering centers are adopted in the following simulations as shown in Fig.9. The VFM ISAR works at the X-band with a carrier frequency of 10GHz and bandwidth of 300MHz. The pulse-band is 100 μs and the pulse repetition frequency is 1 KHz. The length of down range is 256, and length of cross range is 128. The rotary angular velocity of the turntable is 0.05rad/s. We obtain the sparse raw echo data shown in Fig.10. As shown in images, some data are missing in cross range domain, where the number of sampled data is 100.

In order to verify the robustness of the proposed algorithm in sparse aperture echo imaging, different numbers of burst are set in the simulation experiment. Synthetic HRRP through dechirping range compression and compensation are utilized to make a preprocessing, the final ISAR imaging results are shown in Fig.11, where the number of sampled data are 100, 64 and 32 in Fig.11 (1), (2) and (3), respectively. In Fig.11(1), FFT is used to achieve azimuthal pulse compression to obtain two-dimensional images. 2D images are obtained by using the traditional compression sensing reconstruction method (l1_ls) in Fig.11(2). Fig.11(3) and (4) are reconstructed by WCS and MWCS respectively. It is obvious that the proposed method has a better performance than other methods with a same SNR level (20dB); even in a few measurement data condition, we also can get a high-quality imaging result and complete details. Conversely, the imaging result achieved by conventional Fourier transform is severely blurring in azimuth because of missing data in azimuth domain.

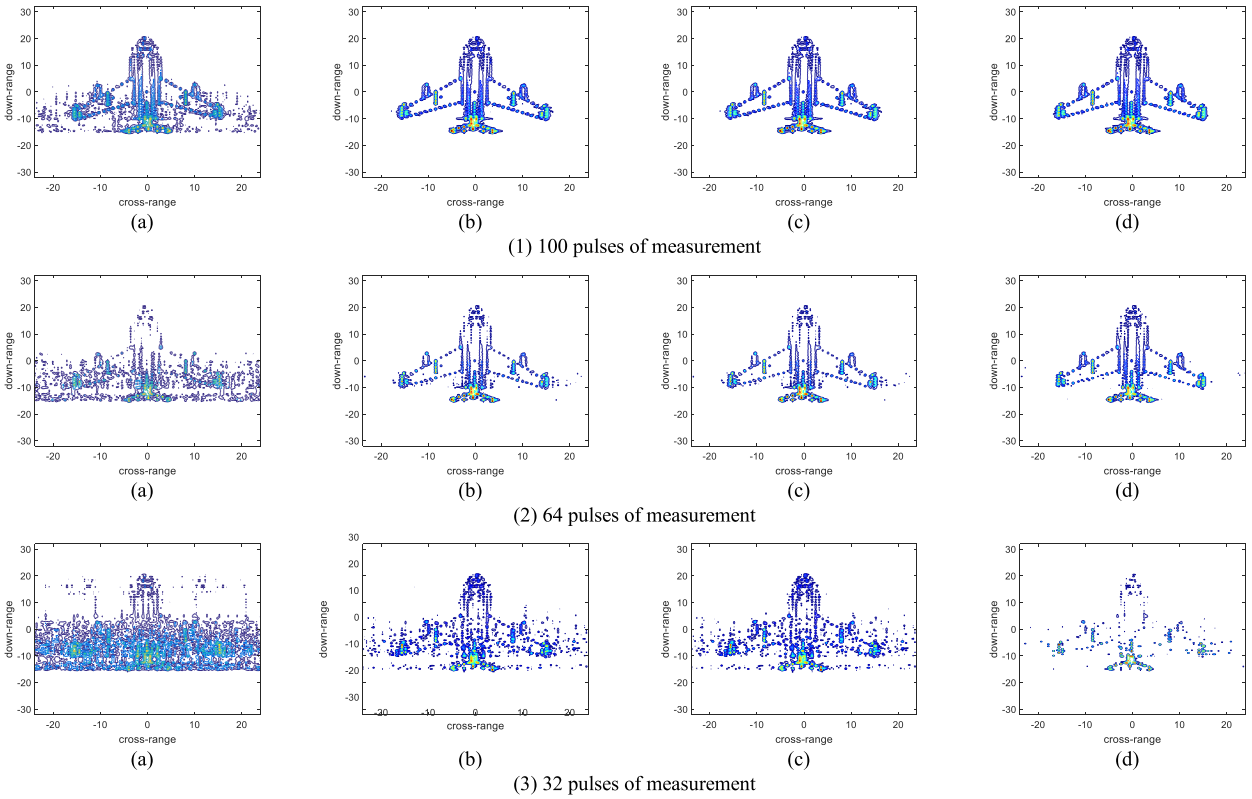

FIGURE 11. ISAR imaging results (a) FT, (b) conventional compressive sensing, (c) WCS (d) MWCS.

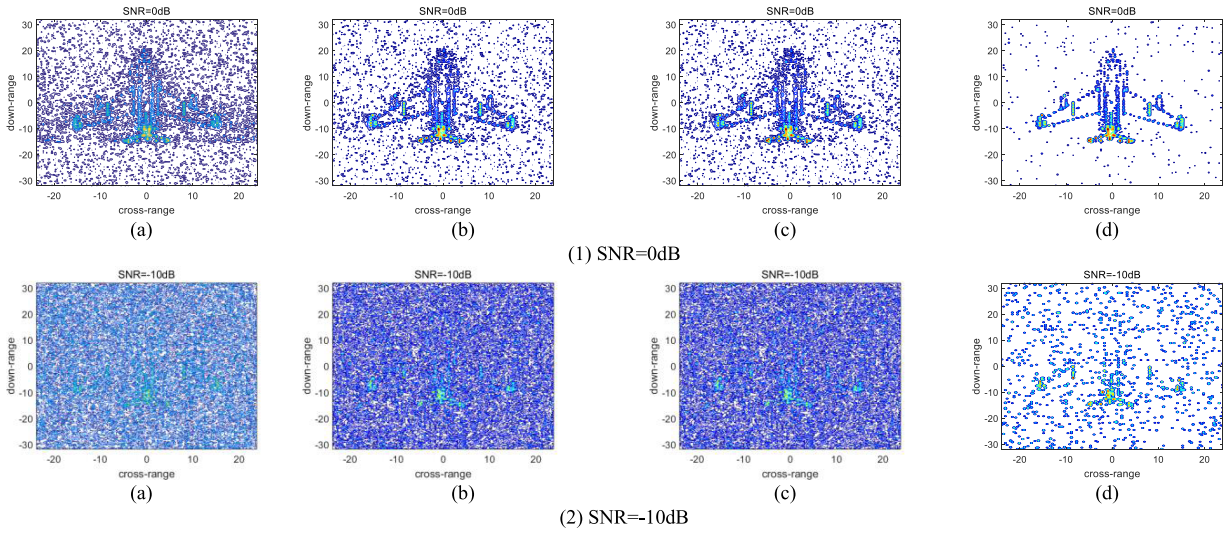

FIGURE 12. ISAR imaging results (a) FT, (b) conventional compressive sensing, (c) WCS (d) MWCS.

Different numbers of sampled signals will result in different imaging effects. When the signal noise ratio is high, the compressed sensing reconstruction methods can obtain high resolution imaging results. Although the MWCS method does not produce defocus in the azimuth direction, the image also loses a lot of detail information, like Fig.11(3) d.

In this experiment, we characterize the performance of ISAR imaging based on MWCS in case of different SNRs. To provide a quantitative evaluation for imaging performance, we establish two indexes related to radar target recognition. The first index is the normalized root mean square error (RMSE) between the reconstructed image and the target model, such as

$$RMSE = \sqrt{\frac{1}{MN}\sum_{m=1}^{M}\sum_{n=1}^{N}(\mathbf{I_1}(m,n) - \mathbf{I_2}(m,n))^2} \quad (30)$$

where $\mathbf{I_1}, \mathbf{I_2}$ denote reference ISAR image and the reconstructed ISAR image with different SNRs.

The another evaluation index is the correlation coefficient (CC) [34], which can be represented by

$$CC = \frac{Cov(\mathbf{I_1}, \mathbf{I_2})}{\sqrt{D(\mathbf{I_1})} \cdot \sqrt{D(\mathbf{I_2})}} \quad (31)$$

where $Cov()$ and $D()$ represent the covariance and variance coefficient between two matrices respectively.

To confirm the effectiveness of our proposed algorithm, we perform experiments under different conditions of signal-to-noise (SNR). MWCS method can obtain better quality images at lower SNR, even SNR $= -10$dB. Different powers of complex Gaussian noise are added to the waveform echo. Consider that the sparsity of echo is sat as 100, we get the imaging results when SNR $= 0$ and -10dB, shown in Fig.12.

Compared with Fig.11 (1), we note that the proposed method has a more stable anti-noise performance. But at the same time the imaging resolution will also be affected, like Fig.12 (2)d, because the support set changes in the weighting process as the noise level increases, which causes some weak scattering point echo signals to be suppressed. As a result, the number of scattered points of imaging is reduced and some details are ignored.

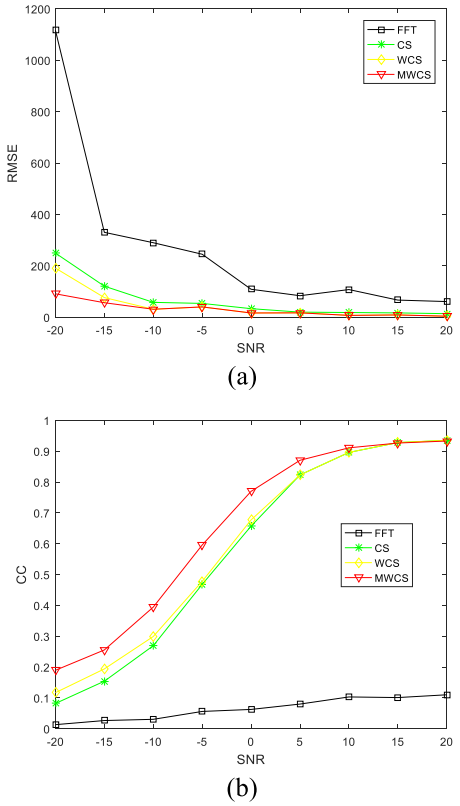

FIGURE 13. Curves of imaging performance under different SNRs. (a) RMSE versus SNR. (b) CC versus SNR.

To characterize the performance quantitatively, the corresponding curves of RMSE and CC are shown in Fig.13. In Fig.13(a), the SNR is varied from -20 to 20dB. Note that the performance of four methods degrades apparently with

the decrease in SNR just as expected. However, compared with FFT, another three methods generate better images quality with a much smaller quantity of reference image under the condition of related high SNRs. In the case of lower SNR, the image quality obtained by MWCS reconstruction is the highest, followed by WCS reconstruction. From Fig.13(b), we can come to a similar conclusion. And we find that when the SNR is higher than 10 dB, the reconstructed images with MWCS, WCS and CS are very close reference image of full aperture. On the other hand, the reconstruction performance of MWCS algorithm is better than other algorithms in the cases of low SNR. It can also be seen from the figure that there is little difference between the imaging effects of CS and WCS, although the WCS algorithm is better under the condition of low SNR.

V. CONCLUSION

VFM waveform avoids the ambiguity appeared in range and velocity, which can improve the resolution of ISAR imaging. But due to the frequency shift and delay, it is necessary to implement pulse compression using dual channels for moving target. Based on previous researches, we establish the sparse VFM waveform echo model in this paper, and propose a modified weighted rule in compressive sensing and the iterative algorithm to get a high-quality recovery image under low SNR condition. The reconstruction algorithm has a better performance than other previous algorithms, through the computational complexity is acceptably increased. The proposed method obtain high resolution ISAR images in experiments with sparse VFM signal under noisy environment.

REFERENCES

[1] V. C. Chen and M. Martorella. *Inverse Synthetic Aperture Radar Imaging: Principles, Algorithms and Applications*. Rijeka, Croatia: SciTech, 2014.

[2] V. C. Chen and W. J. Miceli, "Simulation of ISAR imaging of moving targets," *IEE Proc.-Radar, Sonar Navigat.*, vol. 148, no. 3, pp. 160–166, Jun. 2001.

[3] B. Tian, Z. Lu, Y. Liu, and X. Li, "Review on interferometric ISAR 3D imaging: Concept, technology and experiment," *Signal Process.*, vol. 153, pp. 164–187, Dec. 2018.

[4] Y. Zhu, Y. Su, and W. Yu, "An ISAR imaging method based on MIMO technique," *IEEE Trans. Geosci. Remote Sens.*, vol. 48, no. 8, pp. 3290–3299, Aug. 2010.

[5] D. Pastina, M. Bucciarelli, and P. Lombardo, "Multistatic and MIMO distributed ISAR for enhanced cross-range resolution of rotating targets," *IEEE Trans. Geosci. Remote Sens.*, vol. 48, no. 8, pp. 3300–3317, Aug. 2010.

[6] D.-W. Wang, X.-Y. Ma, A.-L. Chen, and Y. Su, "High-resolution imaging using a wideband MIMO radar system with two distributed arrays," *IEEE Trans. Image Process.*, vol. 19, no. 5, pp. 1280–1289, May 2010.

[7] C. Ma, T. S. Yeo, Y. Zhao, and J. Feng, "MIMO radar 3D imaging based on combined amplitude and total variation cost function with sequential order one negative exponential form," *IEEE Trans. Image Process.*, vol. 23, no. 5, pp. 2168–2183, May 2014.

[8] X. Hu, N. Tong, Y. Zhang, and D. Huang, "MIMO radar imaging with nonorthogonal waveforms based on joint-block sparse recovery," *IEEE Trans. Geosci. Remote Sens.*, vol. 56, no. 10, pp. 5985–5996, Oct. 2018.

[9] K. L. Sitler, M. A. Temple, R. C. Novack, and J. A. Hughes, "High range resolution profiling using phase-coded, stepped-frequency waveforms," *Electron. Lett.*, vol. 38, no. 1, pp. 46–48, Jan. 2002.

[10] K.-T. Kim, "Focusing of high range resolution profiles of moving targets using stepped frequency waveforms," *IET Radar, Sonar Navigat.*, vol. 4, pp. 564–575, Aug. 2010.

[11] X. Zhu, *Radar Signal Analysis and Processing*. Beijing, China: National defense Industry Press, 2011, pp. 143–150.

[12] X.-Y. Pan, W. Wang, and G.-Y. Wang, "Sub-Nyquist sampling jamming against ISAR with CS-based HRRP reconstruction," *IEEE Sensors J.*, vol. 16, no. 6, pp. 1597–1602, Mar. 15, 2016.

[13] J. Pan and X. Cheng, "Comparative analysis of the resolution of VFM signal and chirp-SF signal," *Shipboard Electron. Warfare*, vol. 25, no. 1, pp. 1–3, 2002. doi: 10.3969/j.issn.1673-9167.2002.01.001.

[14] J. Chen, X. Pan, L. Xu, and W. Wang, "Bistatic ISAR imaging with a V-FM waveform based on a dual-channel-coupled 2D-CS algorithm," *Sensors*, vol. 18, no. 9, p. 3082, 2018.

[15] J. Chen, X. Pan, L.-T. Xu, and W. Wang, "Deception jamming against ISAR with coupled two-dimensional compressive sensing via sub-Nyquist sampling," *IEEE Access*, vol. 6, pp. 55693–55700, Oct. 2018.

[16] C.-G. Lee, P.-S. Kang, C.-S. Shih, and L. Sha, "Radar dwell scheduling considering physical characteristics of phased array antenna," in *Proc. 24th IEEE Real-Time Syst. Symp. (RTSS)*, Cancún, Mexico, Dec. 2003, pp. 14–24.

[17] D. Anuradha, P. Barua, A. Singhal, and R. P. S. Rathore, "Programmable radar signal processor for a multi function radar," in *Proc. IEEE Radar Conf.*, Pasadena, CA, USA, May 2009, pp. 1–5.

[18] Y. Chen, Q. Zhang, N. Yuan, Y. Luo, and H. Lou, "An adaptive ISAR-imaging-considered task scheduling algorithm for multi-function phased array radars," *IEEE Trans. Signal Process.*, vol. 63, no. 19, pp. 5096–5110, Oct.1, 2015.

[19] D. L. Donoho, "Compressed sensing," *IEEE Trans. Inf. Theory*, vol. 52, no. 4, pp. 1289–1306, Apr. 2006.

[20] E. J. Candès and M. B. Wakin, "An introduction to compressive sampling," *IEEE Signal Process. Mag.*, vol. 25, no. 2, pp. 21–30, Mar. 2008.

[21] E. J. Candès and T. Tao, "Near-optimal signal recovery from random projections: Universal encoding strategies?" *IEEE Trans. Inf. Theory*, vol. 52, no. 12, pp. 5406–5425, Dec. 2006.

[22] R. Baraniuk and P. Steeghs, "Compressive radar imaging," in *Proc. IEEE Radar Conf.*, Boston, MA, USA, Apr. 2007, pp. 128–133.

[23] M. A. Herman and T. Strohmer, "High-resolution radar via compressed sensing," *IEEE Trans. Signal Process.*, vol. 57, no. 6, pp. 2275–2284, Feb. 2009.

[24] J. H. G. Ender, "On compressive sensing applied to radar," *Signal Process.*, vol. 90, no. 5, pp. 1402–1414, 2010.

[25] X. Pan, J. Liu, J. Chen, Q. Xie, and X. Ai, "Sub-Nyquist sampling jamming against chirp-ISAR with CS-D range compression," *IEEE Sensors J.*, vol. 18, no. 3, pp. 1140–1149, Feb. 2018.

[26] L. Zhang, Z.-J. Qiao, M. Xing, Y. Li, and Z. Bao, "High-resolution ISAR imaging with sparse stepped-frequency waveforms," *IEEE Trans. Geosci. Remote Sens.*, vol. 49, no. 11, pp. 4630–4651, Nov. 2011.

[27] M. S. Kang, S. J. Lee, S. H. Lee, and K. T. Kim, "ISAR imaging of high-speed maneuvering target using gapped stepped-frequency waveform and compressive sensing," *IEEE Trans. Image Process.*, vol. 26, no. 10, pp. 5043–5056, Oct. 2017.

[28] J. A. Tropp and A. C. Gilbert, "Signal recovery from random measurements via orthogonal matching pursuit," *IEEE Trans. Inf. Theory*, vol. 53, no. 12, pp. 4655–4666, Dec. 2007.

[29] H. Wu and S. Wang, "Adaptive sparsity matching pursuit algorithm for sparse reconstruction," *IEEE Signal Process. Lett.*, vol. 19, no. 8, pp. 471–474, Aug. 2012.

[30] E. Candes, M. Wakin, and S. Boyd, "Enhancing sparsity by reweighted ℓ_1 minimization," *J. Fourier Anal. Appl.*, vol. 14, no. 5, pp. 877–905, 2008.

[31] L. Zhang, M. Xing, C.-W. Qiu, J. Li, J. Sheng, Y. Li, and Z. Bao, "Resolution enhancement for inversed synthetic aperture radar imaging under low SNR via improved compressive sensing," *IEEE Trans. Geosci. Remote Sens.*, vol. 48, no. 10, pp. 3824–3838, Oct. 2010.

[32] M. S. Kang, S. H. Lee, K. T. Kim, and J. H. Bae, "Bistatic ISAR imaging and scaling of highly maneuvering target with complex motion via compressive sensing," *IEEE Trans. Aerosp. Electron. Syst.*, vol. 54, no. 6, pp. 2809–2826, Dec. 2018.

[33] S. Zhou, N. Xiu, Y. Wang, L. Kong, and H.-D. Qi, "A null-space-based weighted l1 minimization approach to compressed sensing," *Inf. Inference, J. IMA*, vol. 5, no. 1, pp. 76–102, Mar. 2016.

[34] S. Zhang, W. Zhang, Z. Zong, Z. Tian, and T. S. Yeo, "High-resolution bistatic ISAR imaging based on two-dimensional compressed sensing," *IEEE Trans. Antennas Propag.*, vol. 63, no. 5, pp. 2098–2111, May 2015.